

Measurements of Branching Fractions and Polarization in $B \rightarrow K^* \rho$ Decays

K. Abe,¹⁰ K. Abe,⁴⁶ N. Abe,⁴⁹ I. Adachi,¹⁰ H. Aihara,⁴⁸ M. Akatsu,²⁴ Y. Asano,⁵³
T. Aso,⁵² V. Aulchenko,² T. Aushev,¹⁴ T. Aziz,⁴⁴ S. Bahinipati,⁶ A. M. Bakich,⁴³
Y. Ban,³⁶ M. Barbero,⁹ A. Bay,²⁰ I. Bedny,² U. Bitenc,¹⁵ I. Bizjak,¹⁵ S. Blyth,²⁹
A. Bondar,² A. Bozek,³⁰ M. Bračko,^{22,15} J. Brodzicka,³⁰ T. E. Browder,⁹ M.-C. Chang,²⁹
P. Chang,²⁹ Y. Chao,²⁹ A. Chen,²⁶ K.-F. Chen,²⁹ W. T. Chen,²⁶ B. G. Cheon,⁴
R. Chistov,¹⁴ S.-K. Choi,⁸ Y. Choi,⁴² Y. K. Choi,⁴² A. Chuvikov,³⁷ S. Cole,⁴³
M. Danilov,¹⁴ M. Dash,⁵⁵ L. Y. Dong,¹² R. Dowd,²³ J. Dragic,²³ A. Drutskoy,⁶
S. Eidelman,² Y. Enari,²⁴ D. Epifanov,² C. W. Everton,²³ F. Fang,⁹ S. Fratina,¹⁵
H. Fujii,¹⁰ N. Gabyshev,² A. Garmash,³⁷ T. Gershon,¹⁰ A. Go,²⁶ G. Gokhroo,⁴⁴
B. Golob,^{21,15} M. Grosse Perdekamp,³⁸ H. Guler,⁹ J. Haba,¹⁰ F. Handa,⁴⁷ K. Hara,¹⁰
T. Hara,³⁴ N. C. Hastings,¹⁰ K. Hasuko,³⁸ K. Hayasaka,²⁴ H. Hayashii,²⁵ M. Hazumi,¹⁰
E. M. Heenan,²³ I. Higuchi,⁴⁷ T. Higuchi,¹⁰ L. Hinz,²⁰ T. Hojo,³⁴ T. Hokuue,²⁴ Y. Hoshi,⁴⁶
K. Hoshina,⁵¹ S. Hou,²⁶ W.-S. Hou,²⁹ Y. B. Hsiung,^{29,*} H.-C. Huang,²⁹ T. Igaki,²⁴
Y. Igarashi,¹⁰ T. Iijima,²⁴ A. Imoto,²⁵ K. Inami,²⁴ A. Ishikawa,¹⁰ H. Ishino,⁴⁹ K. Itoh,⁴⁸
R. Itoh,¹⁰ M. Iwamoto,³ M. Iwasaki,⁴⁸ Y. Iwasaki,¹⁰ R. Kagan,¹⁴ H. Kakuno,⁴⁸
J. H. Kang,⁵⁶ J. S. Kang,¹⁷ P. Kapusta,³⁰ S. U. Kataoka,²⁵ N. Katayama,¹⁰ H. Kawai,³
H. Kawai,⁴⁸ Y. Kawakami,²⁴ N. Kawamura,¹ T. Kawasaki,³² N. Kent,⁹ H. R. Khan,⁴⁹
A. Kibayashi,⁴⁹ H. Kichimi,¹⁰ H. J. Kim,¹⁹ H. O. Kim,⁴² Hyunwoo Kim,¹⁷ J. H. Kim,⁴²
S. K. Kim,⁴¹ T. H. Kim,⁵⁶ K. Kinoshita,⁶ P. Koppenburg,¹⁰ S. Korpar,^{22,15} P. Krizan,^{21,15}
P. Krokovny,² R. Kulasiri,⁶ C. C. Kuo,²⁶ H. Kurashiro,⁴⁹ E. Kurihara,³ A. Kusaka,⁴⁸
A. Kuzmin,² Y.-J. Kwon,⁵⁶ J. S. Lange,⁷ G. Leder,¹³ S. E. Lee,⁴¹ S. H. Lee,⁴¹
Y.-J. Lee,²⁹ T. Lesiak,³⁰ J. Li,⁴⁰ A. Limosani,²³ S.-W. Lin,²⁹ D. Liventsev,¹⁴
J. MacNaughton,¹³ G. Majumder,⁴⁴ F. Mandl,¹³ D. Marlow,³⁷ T. Matsuiishi,²⁴
H. Matsumoto,³² S. Matsumoto,⁵ T. Matsumoto,⁵⁰ A. Matyja,³⁰ Y. Mikami,⁴⁷
W. Mitaroff,¹³ K. Miyabayashi,²⁵ Y. Miyabayashi,²⁴ H. Miyake,³⁴ H. Miyata,³² R. Mizuk,¹⁴
D. Mohapatra,⁵⁵ G. R. Moloney,²³ G. F. Moorhead,²³ T. Mori,⁴⁹ A. Murakami,³⁹
T. Nagamine,⁴⁷ Y. Nagasaka,¹¹ T. Nakadaira,⁴⁸ I. Nakamura,¹⁰ E. Nakano,³³ M. Nakao,¹⁰
H. Nakazawa,¹⁰ Z. Natkaniec,³⁰ K. Neichi,⁴⁶ S. Nishida,¹⁰ O. Nitoh,⁵¹ S. Noguchi,²⁵
T. Nozaki,¹⁰ A. Ogawa,³⁸ S. Ogawa,⁴⁵ T. Ohshima,²⁴ T. Okabe,²⁴ S. Okuno,¹⁶
S. L. Olsen,⁹ Y. Onuki,³² W. Ostrowicz,³⁰ H. Ozaki,¹⁰ P. Pakhlov,¹⁴ H. Palka,³⁰
C. W. Park,⁴² H. Park,¹⁹ K. S. Park,⁴² N. Parslow,⁴³ L. S. Peak,⁴³ M. Pernicka,¹³
J.-P. Perroud,²⁰ M. Peters,⁹ L. E. Piilonen,⁵⁵ A. Poluektov,² F. J. Ronga,¹⁰ N. Root,²
M. Rozanska,³⁰ H. Sagawa,¹⁰ M. Saigo,⁴⁷ S. Saitoh,¹⁰ Y. Sakai,¹⁰ H. Sakamoto,¹⁸
T. R. Sarangi,¹⁰ M. Satapathy,⁵⁴ N. Sato,²⁴ O. Schneider,²⁰ J. Schümann,²⁹ C. Schwanda,¹³
A. J. Schwartz,⁶ T. Seki,⁵⁰ S. Semenov,¹⁴ K. Senyo,²⁴ Y. Settai,⁵ R. Seuster,⁹
M. E. Sevier,²³ T. Shibata,³² H. Shibuya,⁴⁵ B. Shwartz,² V. Sidorov,² V. Siegle,³⁸
J. B. Singh,³⁵ A. Somov,⁶ N. Soni,³⁵ R. Stamen,¹⁰ S. Stanič,^{53,†} M. Starič,¹⁵ A. Sugi,²⁴
A. Sugiyama,³⁹ K. Sumisawa,³⁴ T. Sumiyoshi,⁵⁰ S. Suzuki,³⁹ S. Y. Suzuki,¹⁰ O. Tajima,¹⁰
F. Takasaki,¹⁰ K. Tamai,¹⁰ N. Tamura,³² K. Tanabe,⁴⁸ M. Tanaka,¹⁰ G. N. Taylor,²³

Y. Teramoto,³³ X. C. Tian,³⁶ S. Tokuda,²⁴ S. N. Tovey,²³ K. Trabelsi,⁹ T. Tsuboyama,¹⁰
T. Tsukamoto,¹⁰ K. Uchida,⁹ S. Uehara,¹⁰ T. Uglov,¹⁴ K. Ueno,²⁹ Y. Unno,³ S. Uno,¹⁰
Y. Ushiroda,¹⁰ G. Varner,⁹ K. E. Varvell,⁴³ S. Villa,²⁰ C. C. Wang,²⁹ C. H. Wang,²⁸
J. G. Wang,⁵⁵ M.-Z. Wang,²⁹ M. Watanabe,³² Y. Watanabe,⁴⁹ L. Widhalm,¹³
Q. L. Xie,¹² B. D. Yabsley,⁵⁵ A. Yamaguchi,⁴⁷ H. Yamamoto,⁴⁷ S. Yamamoto,⁵⁰
T. Yamanaka,³⁴ Y. Yamashita,³¹ M. Yamauchi,¹⁰ Heyoung Yang,⁴¹ P. Yeh,²⁹ J. Ying,³⁶
K. Yoshida,²⁴ Y. Yuan,¹² Y. Yusa,⁴⁷ H. Yuta,¹ S. L. Zang,¹² C. C. Zhang,¹² J. Zhang,¹⁰
L. M. Zhang,⁴⁰ Z. P. Zhang,⁴⁰ V. Zhilich,² T. Ziegler,³⁷ D. Žontar,^{21,15} and D. Zürcher²⁰

(The Belle Collaboration)

¹*Aomori University, Aomori*

²*Budker Institute of Nuclear Physics, Novosibirsk*

³*Chiba University, Chiba*

⁴*Chonnam National University, Kwangju*

⁵*Chuo University, Tokyo*

⁶*University of Cincinnati, Cincinnati, Ohio 45221*

⁷*University of Frankfurt, Frankfurt*

⁸*Gyeongsang National University, Chinju*

⁹*University of Hawaii, Honolulu, Hawaii 96822*

¹⁰*High Energy Accelerator Research Organization (KEK), Tsukuba*

¹¹*Hiroshima Institute of Technology, Hiroshima*

¹²*Institute of High Energy Physics,*

Chinese Academy of Sciences, Beijing

¹³*Institute of High Energy Physics, Vienna*

¹⁴*Institute for Theoretical and Experimental Physics, Moscow*

¹⁵*J. Stefan Institute, Ljubljana*

¹⁶*Kanagawa University, Yokohama*

¹⁷*Korea University, Seoul*

¹⁸*Kyoto University, Kyoto*

¹⁹*Kyungpook National University, Taegu*

²⁰*Swiss Federal Institute of Technology of Lausanne, EPFL, Lausanne*

²¹*University of Ljubljana, Ljubljana*

²²*University of Maribor, Maribor*

²³*University of Melbourne, Victoria*

²⁴*Nagoya University, Nagoya*

²⁵*Nara Women's University, Nara*

²⁶*National Central University, Chung-li*

²⁷*National Kaohsiung Normal University, Kaohsiung*

²⁸*National United University, Miao Li*

²⁹*Department of Physics, National Taiwan University, Taipei*

³⁰*H. Niewodniczanski Institute of Nuclear Physics, Krakow*

³¹*Nihon Dental College, Niigata*

³²*Niigata University, Niigata*

³³*Osaka City University, Osaka*

³⁴*Osaka University, Osaka*

³⁵*Panjab University, Chandigarh*

³⁶*Peking University, Beijing*

- ³⁷*Princeton University, Princeton, New Jersey 08545*
³⁸*RIKEN BNL Research Center, Upton, New York 11973*
³⁹*Saga University, Saga*
⁴⁰*University of Science and Technology of China, Hefei*
⁴¹*Seoul National University, Seoul*
⁴²*Sungkyunkwan University, Suwon*
⁴³*University of Sydney, Sydney NSW*
⁴⁴*Tata Institute of Fundamental Research, Bombay*
⁴⁵*Toho University, Funabashi*
⁴⁶*Tohoku Gakuin University, Tagajo*
⁴⁷*Tohoku University, Sendai*
⁴⁸*Department of Physics, University of Tokyo, Tokyo*
⁴⁹*Tokyo Institute of Technology, Tokyo*
⁵⁰*Tokyo Metropolitan University, Tokyo*
⁵¹*Tokyo University of Agriculture and Technology, Tokyo*
⁵²*Toyama National College of Maritime Technology, Toyama*
⁵³*University of Tsukuba, Tsukuba*
⁵⁴*Utkal University, Bhubaneswer*
⁵⁵*Virginia Polytechnic Institute and State University, Blacksburg, Virginia 24061*
⁵⁶*Yonsei University, Seoul*

Abstract

We present results of a study of the charmless vector-vector decays $B^0 \rightarrow K^{*0}\rho^0$ and $B^+ \rightarrow K^{*0}\rho^+$. The results are based on a 140 fb^{-1} data sample collected by the Belle detector at the KEKB asymmetric e^+e^- collider. We obtain the branching fraction $\mathcal{B}(B^+ \rightarrow K^{*0}\rho^+) = (6.6 \pm 2.2(\text{stat.}) \pm 0.8(\text{syst.})) \times 10^{-6}$, and set upper limits on the branching fractions $\mathcal{B}(B^0 \rightarrow K^{*0}\rho^0) < 2.6 \times 10^{-6}$ and $\mathcal{B}(B^0 \rightarrow f_0(980)K^{*0}) < 5.2 \times 10^{-6}$. We also perform a helicity analysis of the ρ and K^* vector mesons in the decay $B^+ \rightarrow K^{*0}\rho^+$, and obtain the longitudinal polarization fraction $R_0(B^+ \rightarrow K^{*0}\rho^+) = 0.50 \pm 0.19(\text{stat.})^{+0.05}_{-0.07}(\text{syst.})$.

PACS numbers: 13.25.Hw, 14.40.Nd.

In addition to rate asymmetries, $B \rightarrow VV$ decays provide opportunities to search for direct CP and/or T violation [1] and new physics [2] through angular correlations between the vector meson decay final states. These decays produce final states where three helicity states are possible, whose amplitudes are called A_0 , A_+ and A_- in the helicity basis. The Standard Model (SM) with factorization predicts $R_0 \gg R_T$ [3, 4], where $R_0 = |A_0|^2/(|A_0|^2 + |A_+|^2 + |A_-|^2)$ ($R_T = (|A_+|^2 + |A_-|^2)/(|A_0|^2 + |A_+|^2 + |A_-|^2)$) is the longitudinal (transverse) polarization fraction. In the tree-dominated $B^+ \rightarrow \rho^+ \rho^0$, this prediction is confirmed [5, 6]. In contrast, for the $B \rightarrow \phi K^*$ decay, which is a pure $b \rightarrow s$ penguin transition, Belle [7] and Babar [6] find $R_0 \approx R_T$, which is in disagreement with SM predictions. It is thus important to obtain polarization measurements in other VV modes, such as $B \rightarrow K^* \rho$ and, in particular, in the pure penguin $b \rightarrow s \bar{d} d$ decay, $B^+ \rightarrow K^{*0} \rho^+$.

In this paper, we present the results of a study of $B^0 \rightarrow K^{*0} \rho^0$ and $B^+ \rightarrow K^{*0} \rho^+$ decays with a 140 fb^{-1} data sample containing 152×10^6 B meson pairs collected with the Belle detector at the KEKB asymmetric-energy e^+e^- collider [8] operating at the $\Upsilon(4S)$ resonance ($\sqrt{s} = 10.58 \text{ GeV}$). The production rates for B^+B^- and $B^0\bar{B}^0$ pairs are assumed to be equal.

The Belle detector is a large solid-angle magnetic spectrometer that consists of a three-layer silicon vertex detector (SVD), a 50-layer central drift chamber (CDC), an array of aerogel threshold Čerenkov counters (ACC), a barrel-like arrangement of time-of-flight scintillation counters (TOF), and an electromagnetic calorimeter comprised of CsI(Tl) crystals (ECL) located inside a super-conducting solenoid coil that provides a 1.5 T magnetic field. An iron flux-return located outside of the coil is instrumented to detect K_L^0 mesons and to identify muons (KLM). The detector is described in detail elsewhere [9].

We select $B \rightarrow K^* \rho$ candidate events by combining four charged tracks (three pions plus one kaon) or three charged tracks (two pions plus one kaon) and one neutral pion. Each charged track is required to have a transverse momentum $p_T > 0.1 \text{ GeV}/c$ and to have an origin within 0.2 cm in the radial direction and 5 cm along the beam direction of the interaction point (IP).

Particle identification likelihoods for the pion and kaon particle hypotheses are calculated by combining information from the TOF and ACC systems with dE/dx measurements in the CDC. To identify kaons, we require the kaon likelihood ratio, $L_K/(L_K + L_\pi)$, to be greater than 0.6. To identify pions, we require $L_K/(L_K + L_\pi)$ to be less than 0.4. In addition, charged tracks are rejected if they are consistent with the electron hypothesis.

Candidate π^0 mesons are reconstructed from pairs of photons that have an invariant mass in the range $0.1178 - 0.1502 \text{ GeV}/c^2$, corresponding to a window of $\pm 3\sigma$ around the nominal π^0 mass, where the photons are assumed to originate from the IP. The energy of each photon in the laboratory frame is required to be greater than 50 MeV for the ECL barrel region ($32^\circ < \theta < 129^\circ$) and 100 MeV for the ECL endcap regions ($17^\circ < \theta < 32^\circ$ or $129^\circ < \theta < 150^\circ$), where θ denotes the polar angle of the photon with respect to the beam line. The π^0 candidates are kinematically constrained to the nominal π^0 mass. In order to reduce the combinatorial background, we only accept π^0 candidates with momenta $p_{\pi^0} > 0.40 \text{ GeV}/c$ in the e^+e^- center-of-mass system (CMS).

Candidate ρ mesons are reconstructed via their $\rho^0 \rightarrow \pi^+\pi^-$ and $\rho^+ \rightarrow \pi^+\pi^0$ decays. For both the charged and neutral modes, we require $0.62 \text{ GeV}/c^2 < M(\pi\pi) < 0.92 \text{ GeV}/c^2$. We select $K^{*0} \rightarrow K^+\pi^-$ decay candidates with invariant masses in the range $0.84 \text{ GeV}/c^2 < M(K^+\pi^-) < 0.94 \text{ GeV}/c^2$ for $K^{*0} \rho^0$ and $0.83 \text{ GeV}/c^2 < M(K^+\pi^-) < 0.97 \text{ GeV}/c^2$ for $K^{*0} \rho^+$.

To isolate the signal, we form the beam-constrained mass $M_{bc} \equiv \sqrt{E_{\text{beam}}^2 - p_B^2}$, and the

energy difference $\Delta E \equiv E_B - E_{\text{beam}}$, where E_{beam} is the CMS beam energy, and p_B and E_B are the CMS momentum and energy, respectively, of the B candidate. We accept events in the region defined by $M_{bc} > 5.2 \text{ GeV}/c^2$ and $-0.4 \text{ GeV} < \Delta E < 0.4 \text{ GeV}$. Within this accepted range we further define mode-dependent signal regions. For $B^0 \rightarrow K^{*0}\rho^0$, the ΔE signal region is $-0.04 \text{ GeV} < \Delta E < 0.04 \text{ GeV}$. For $B^+ \rightarrow K^{*0}\rho^+$, the ΔE distribution has a tail on the lower side caused by incomplete longitudinal containment of electromagnetic showers in the CsI(Tl) crystals, so the ΔE signal region is broadened to $-0.10 \text{ GeV} < \Delta E < 0.06 \text{ GeV}$. For both decays, the M_{bc} signal region is $5.27 \text{ GeV}/c^2 < M_{bc} < 5.29 \text{ GeV}/c^2$. These requirements correspond to approximately $\pm 3\sigma$ for both quantities.

The continuum process $e^+e^- \rightarrow q\bar{q}$ ($q = u, d, s, c$) is the main source of background and must be strongly suppressed. One method of discriminating the signal from background is based on the event topology, which tends to be isotropic for $B\bar{B}$ events and jet-like for $q\bar{q}$ events. Another discriminating characteristic is θ_B , the CMS polar angle of the B flight direction. B mesons are produced with a $1 - \cos^2 \theta_B$ distribution while continuum background events tend to be uniform in $\cos \theta_B$. For $B^0 \rightarrow K^{*0}\rho^0$, we require $|\cos \theta_{\text{thr}}| < 0.8$, where θ_{thr} is the angle between the thrust axis of the candidate tracks and that of the remaining tracks in the event. This distribution is flat for signal events and peaked at $\cos \theta_{\text{thr}} = \pm 1$ for continuum background.

We use Monte Carlo (MC) simulated signal and continuum events to form a Fisher discriminant based on modified Fox-Wolfram moments [10] that are verified to be uncorrelated with M_{bc} , ΔE and variables considered later in the analysis. Probability density functions (PDFs) derived from the Fisher discriminant and the $\cos \theta_B$ distributions are multiplied to form likelihood functions for signal (\mathcal{L}_s) and continuum ($\mathcal{L}_{q\bar{q}}$); these are combined into a likelihood ratio $\mathcal{R}_s = \mathcal{L}_s/(\mathcal{L}_s + \mathcal{L}_{q\bar{q}})$. Additional discrimination is provided by the b -flavor tagging parameter r , which ranges from 0 to 1 and is a measure of the likelihood that the b flavor of the accompanying B meson is correctly assigned by the Belle flavor-tagging algorithm [11]. Events with high values of r are well-tagged and are less likely to originate from continuum production. We define a multi-dimensional likelihood ratio $\mathcal{M} = \mathcal{L}_s^{\text{MDLR}}/(\mathcal{L}_s^{\text{MDLR}} + \mathcal{L}_{q\bar{q}}^{\text{MDLR}})$, where $\mathcal{L}_s^{\text{MDLR}}$ denotes the likelihood determined by the r - \mathcal{R}_s distribution for signal and $\mathcal{L}_{q\bar{q}}^{\text{MDLR}}$ is that for the continuum background. We determine \mathcal{M} cut by optimizing the figure of merit, $S/\sqrt{(S+B)}$, where B is the number of background events and S is the number of signal events. We require $\mathcal{M} > 0.85$ for $K^{*0}\rho^0$ and $\mathcal{M} > 0.95$ for $K^{*0}\rho^+$.

To investigate backgrounds from other B decays, we use a sample of $B\bar{B}$ MC events corresponding to an integrated luminosity of 412 fb^{-1} . We find background from $B^+ \rightarrow \bar{D}^0(K^{*0}\pi^0)\pi^+$ in the ρ sideband region. We apply the requirement $|M(K\pi^+\pi^0) - M_{D^0}| > 0.050 \text{ GeV}/c^2$ to veto those events. This requirement does not remove any $B^+ \rightarrow K^{*0}\rho^+$ events. The $B^0 \rightarrow K^{*0}\rho^0$ mode includes vetoes on $B^0 \rightarrow D^-(K^-\pi^+\pi^-)\pi^+$, $B^0 \rightarrow D^{*(2010)-}(D^0\pi^-)\pi^+$ and $B^0 \rightarrow D_2^{*(2460)-}(D^0\pi^-)\pi^+$. The cuts $|M(K\pi\pi) - M_{D^0}| > 0.050 \text{ GeV}/c^2$, $|M(K\pi\pi) - M_{D^{*(2010)}}| > 0.050 \text{ GeV}/c^2$ and $|M(K\pi\pi) - M_{D_2^{*(2460)}}| > 0.060 \text{ GeV}/c^2$ eliminate these backgrounds.

After all the event selection requirements are applied, there is no significant peaking background in either ΔE or M_{bc} for $B^+ \rightarrow K^{*0}\rho^+$. For $B^0 \rightarrow K^{*0}\rho^0$ we find some broadly peaking 3-body and 5-body rare decays above and below the signal in the ΔE distribution. These shapes are included in the M_{bc} - ΔE fit for this mode. A further cut, $\Delta E > -0.2 \text{ GeV}$, is also applied to eliminate most of the remaining 5-body background.

In the $B^+ \rightarrow K^{*0}\rho^+$ M_{bc} - ΔE signal region, we find that the fraction of multiple candi-

dates is 3.5% for the $|A_0|^2$ helicity state and 1.6% for the $|A_\pm|^2$ state. We allow for multiple candidates in this mode. For $B^0 \rightarrow K^{*0}\rho^0$ the wide mass windows result in many multiple candidates; we choose the entry that has the minimum χ^2 from the vertex constrained fit.

We extract the signal yield by applying an extended unbinned maximum-likelihood fit to the two-dimensional M_{bc} - ΔE distribution. The fit includes components for signal plus backgrounds from continuum events and $b \rightarrow c$ decays. The signal PDF is represented by a Gaussian function for M_{bc} and either a double Gaussian (for the $K^{*0}\rho^0$ mode) or a “Crystal Ball” line shape function [12] (for the $K^{*0}\rho^+$ mode) for ΔE . The shape parameters are determined from fits to MC. The signal PDF is adjusted to account for small differences observed between data and MC. The $B^0 \rightarrow K^{*0}\rho^0$ signal PDF is calibrated with $B^0 \rightarrow D^0(K^-\pi^+\pi^-\pi^+)\pi^+$; the $B^+ \rightarrow K^{*0}\rho^+$ PDF is calibrated with high-statistics modes containing π^0 mesons, i.e., $B^+ \rightarrow \bar{D}^0(K^+\pi^-\pi^0)\pi^+$. The continuum PDF is described by a product of a threshold (ARGUS) function [13] for M_{bc} and a first-order polynomial for ΔE , with shape parameters allowed to vary. The PDF for $b \rightarrow c$ decay is modeled by a smoothed two-dimensional histogram obtained from a large MC sample. In addition, the $B^0 \rightarrow K^{*0}\rho^0$ fit contains PDFs for the dominant rare 3-body ($B^0 \rightarrow K^{*0}\pi$) and 5-body ($B^0 \rightarrow a_1 K^{*0}$) decays, modeled by smoothed two-dimensional histograms.

Figure 1 shows the fit results. We find 14.1 ± 4.4 $B^0 \rightarrow K^+\pi^-\pi^+\pi^-$ events and 56.5 ± 11.6 $B^+ \rightarrow K^+\pi^-\pi^+\pi^0$ events. The corresponding statistical significance of the signal, defined as $\sqrt{-2\ln(\mathcal{L}_0/\mathcal{L}_{\max})}$, where \mathcal{L}_{\max} is the likelihood value at the best-fit signal yield and \mathcal{L}_0 is the value with the signal yield set to zero, is 5.0σ or 6.3σ .

The $M_{bc} - \Delta E$ fits do not distinguish signal from non-resonant decays, such as $B \rightarrow \rho K\pi$ or $B \rightarrow K^*\pi\pi$, which contain the same final state particles. Therefore, we extract the $K^*\rho$ signal yield by fitting the $M(\pi\pi)$ and $M(K\pi)$ invariant masses for events in the M_{bc} and ΔE signal region.

For $B^0 \rightarrow K^{*0}\rho^0$ signal region events, we perform a two-dimensional maximum likelihood fit in the range $0.5 \text{ GeV}/c^2 < M(K^+\pi^-) < 1.2 \text{ GeV}/c^2$ and $0.5 \text{ GeV}/c^2 < M(\pi^+\pi^-) < 1.2 \text{ GeV}/c^2$. The distribution for these events is shown in Fig. 2. From this distribution it is clear there are significant contributions from non-resonant backgrounds. The signal PDF is modeled by the product of Breit-Wigner functions for both the ρ^0 and K^{*0} resonances with means and widths determined from the MC simulation. The continuum and $b \rightarrow c$ fractions are each modeled by a smoothed two-dimensional histogram determined from MC. Three main non-resonant decays are considered in this fit: $B^0 \rightarrow K^{*0}\pi^+\pi^-$, $B^0 \rightarrow K_1(1400)^+(K^{*0}\pi^+)\pi^-$ and $B^0 \rightarrow \rho^0 K^-\pi^+$. The $K^{*0}\pi^+\pi^-$ and $\rho^0 K^-\pi^+$ components are represented as a Breit-Wigner function for the resonance, multiplied by a second order polynomial fit to the non-resonant phase space, determined from MC. The $K_1(1400)^+\pi^-$ component is modeled by a smoothed histogram. From the data mass distribution it is apparent that an additional component to model the $B^0 \rightarrow f_0(980)K^{*0}$ decay is needed. This is represented by the product of two Breit-Wigner functions for the K^{*0} and $f_0(980)$ resonance. The K^{*0} mean and width are determined from MC. The $f_0(980)$ mean and width are allowed to float within the range of values reported in the PDG [14]. The continuum and $b \rightarrow c$ backgrounds are fixed at the levels determined from the $M_{bc} - \Delta E$ fit; the other components are allowed to float. The projections of the fit are shown in Fig. 3. Table I lists the results of the fit. The statistical significance of the $f_0(980)K^{*0}$ signal is 2.8σ .

For $B^+ \rightarrow K^{*0}\rho^+$, we fit $M(\pi\pi)$ in the K^* signal region and $M(K\pi)$ in the ρ signal region simultaneously. Figure 3 (bottom) shows the fit result. The solid curve shows the result of a binned maximum-likelihood fit with four components: signal, background from

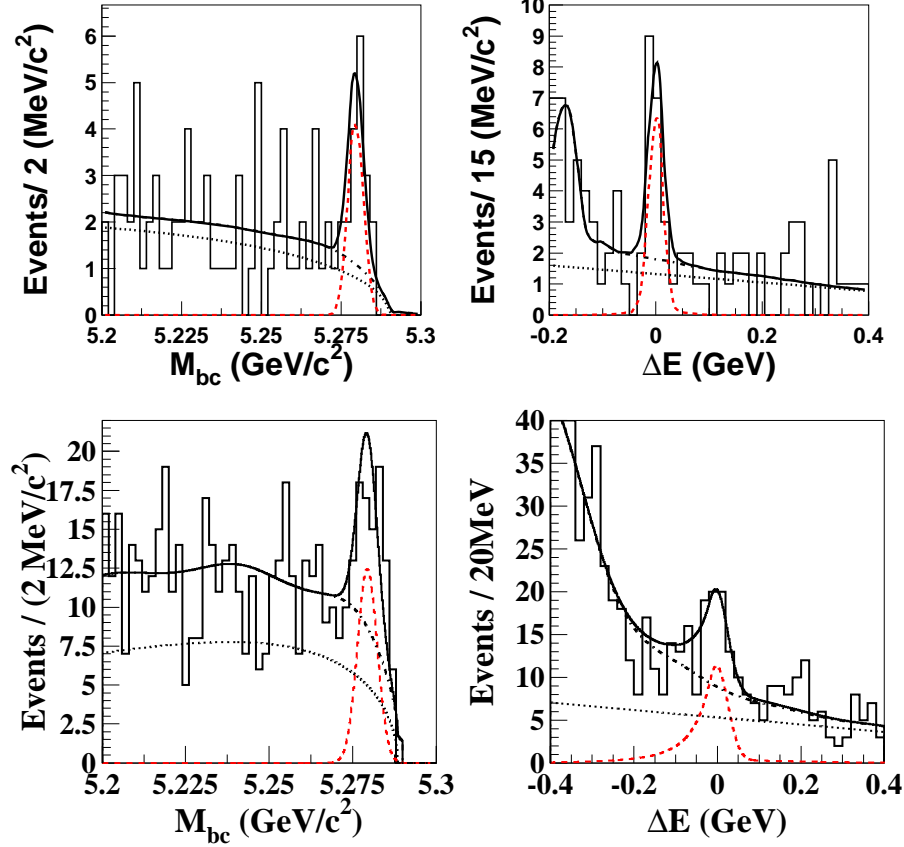


FIG. 1: Projections of M_{bc} for events in the ΔE signal region (left), and projection of ΔE in the M_{bc} signal region (right). The upper plots are for $B^0 \rightarrow K^{*0} \rho^0$, the lower plots for $B^+ \rightarrow K^{*0} \rho^+$. The solid curves show the results of the fits. The dotted lines represent the continuum background. The sum of $b \rightarrow c$ and continuum background component is shown as dashed lines.

continuum and $B\bar{B}$, and non-resonant $\rho K\pi$ and $K^{*0}\pi\pi$. The signal ρ and K^{*0} components are represented by Breit-Wigner functions with masses and widths determined from MC simulation. The background from continuum and $B\bar{B}$ is described by a threshold function plus a Breit-Wigner function for $M(\pi^+\pi^0)$, a threshold function plus a Gaussian and a Breit-Wigner function for $M(K^+\pi^-)$, where a resonant component is included to account for resonance production in the continuum. The shape parameters are determined from sideband data. The non-resonant $\rho K\pi$ and $K^*\pi\pi$ components are represented by threshold functions with parameters determined from a MC simulation with the final state particles distributed uniformly over phase space. In the fit, the yield for each component in the ρ or K^{*0} signal region is required to be the same. All normalizations are allowed to float, except for the background from continuum and $B\bar{B}$, which is fixed at the M_{bc} - ΔE fit results. Table II lists the yields in the ρ^+ and K^{*0} mass window. The statistical significance of the $B^+ \rightarrow K^{*0} \rho^+$ signal is 3.2σ .

We use the $\rho^+ \rightarrow \pi^+\pi^0$ and $K^{*0} \rightarrow K^+\pi^-$ helicity-angle (θ_{hel}) distributions to determine the relative strengths of $|A_0|^2$ and $|A_{\pm}|^2$. Here θ_{hel} is the angle between an axis anti-parallel to the B flight direction and the π^+ (K^+) flight direction in the ρ^+ (K^*) rest frame. For the longitudinal polarization case, the distribution is proportional to $\cos^2 \theta_{\text{hel}(\rho)} \cos^2 \theta_{\text{hel}(K^*)}$ and,

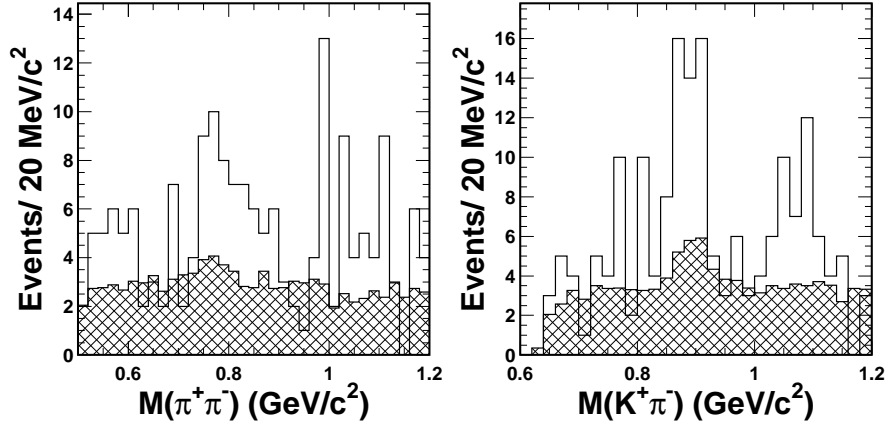


FIG. 2: Distributions of $M(\pi^+\pi^-)$ (left) and $M(K^+\pi^-)$ (right) in the $K^{*0}\rho^0$ signal region (open histogram) and M_{bc} sideband (hatched histogram). Peaks for ρ^0 and K^{*0} can clearly be seen and a sharp peak for the $f_0(980)$ is apparent. Significant contributions of non-resonant background are also seen.

TABLE I: Results of fit to invariant mass for $B^0 \rightarrow K^{*0}\rho^0$. The yields are the number of events over the whole $M(\pi\pi) - M(K\pi)$ region.

$K^{*0}\rho^0$	$f_0(980)K^{*0}$	$\rho K\pi$	$K^{*0}\pi\pi$	$K_1\pi$	$ A_0 ^2$ effc.(%)	$ A_{\pm} ^2$ effc.(%)
0 ± 5.2	$10.2^{+5.3}_{-4.4}$	$30.5^{+10.7}_{-9.8}$	$22.4^{+13.0}_{-12.2}$	$9.4^{+9.4}_{-8.6}$	1.9	3.4

for the transverse polarization case, is proportional to $\sin^2 \theta_{\text{hel}(\rho)} \sin^2 \theta_{\text{hel}(K^*)}$, where $\theta_{\text{hel}(\rho)}$ ($\theta_{\text{hel}(K^*)}$) is the helicity angle for ρ (K^*). Figure 4 shows the distributions of the cosine of the helicity angle for ρ and for K^* for events in the M_{bc} and ΔE signal region. We perform a two-dimensional unbinned maximum likelihood fit to the ρ and K^* helicity distributions. The fit includes components for signal, backgrounds from continuum and $B\bar{B}$ and non-resonant $\rho K\pi$. The $K^*\pi\pi$ component obtained from the invariant mass fit is small and is not included in the helicity fit. PDFs for signal $|A_0|^2$, $|A_{\pm}|^2$ helicity states are determined from the MC simulation. The PDF for background from continuum and $B\bar{B}$ is obtained

TABLE II: Results of fit to invariant mass for $B^+ \rightarrow K^{*0}\rho^+$, together with the MC-determined efficiencies for $|A_0|^2$ and $|A_{\pm}|^2$ states. The yields are the number of events in the K^* and ρ mass window.

$K^{*0}\rho^+$	$\rho K\pi$	$K^*\pi\pi$	$ A_0 ^2$ effc.(%)	$ A_{\pm} ^2$ effc.(%)
26.6 ± 8.7	12.8 ± 3.3	0.6 ± 3.7	2.0	3.3

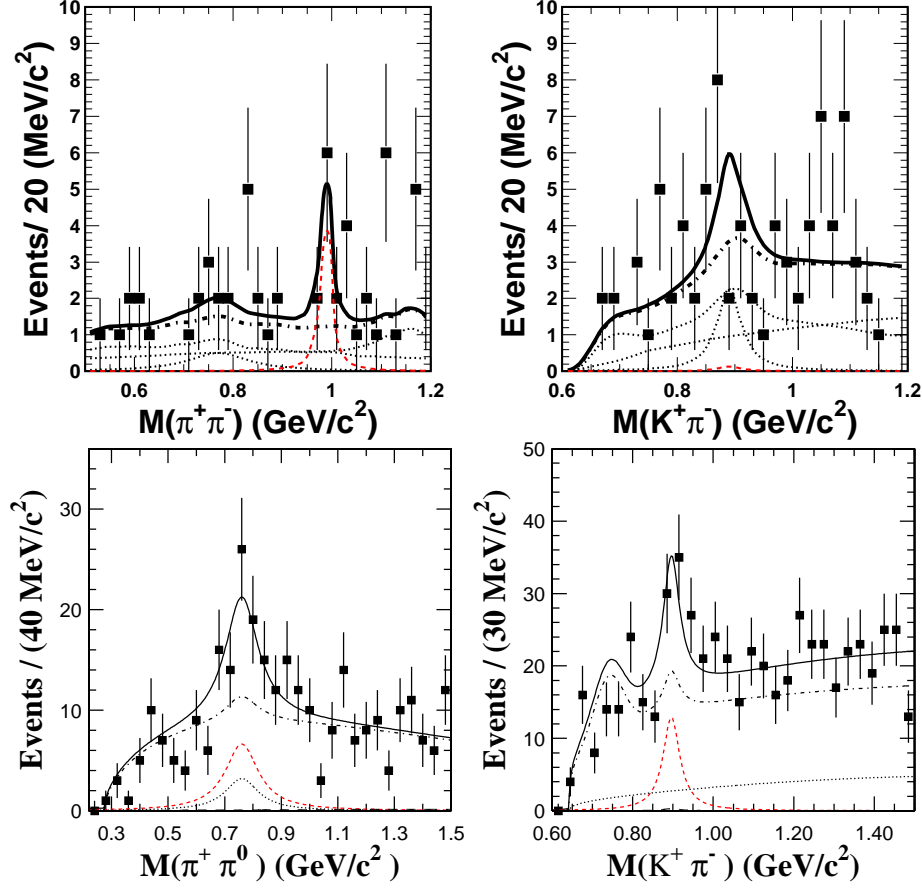


FIG. 3: The upper plots are for $B^0 \rightarrow K^{*0}\rho^0$, $M(\pi^+\pi^-)$ (left) in the K^{*0} signal region and $M(K^+\pi^-)$ in the ρ signal region (right). Solid curves show fit results. Dotted lines show continuum and non-resonant components, red dashed line shows the $f_0(980)K^{*0}$ component. The lower plots are for $B^+ \rightarrow K^{*0}\rho^+$, $M(\pi^+\pi^0)$ (left) in the K^{*0} signal region and $M(K^+\pi^-)$ in the ρ signal region (right). The solid curves show the results of the fit. The signal (continuum, $\rho K\pi$, $K^{*0}\pi\pi$) component is shown as a red dashed (dot-dashed, dotted, dashed) line.

from sideband data. The $\rho K\pi$ PDF is determined by fitting the helicity distribution for events in the region $1.0 \text{ GeV}/c^2 < M(K\pi) < 1.5 \text{ GeV}/c^2$; it is consistent with a $\cos^2 \theta_{\text{hel}}$ -like $\cos \theta(\rho)$ helicity and a flat $\cos \theta(K\pi)$ distribution. The fit result, shown as the solid histogram, gives $R_0 = 0.50 \pm 0.19$; 3.2σ away from 100% longitudinal polarization.

We obtain the longitudinal polarization fraction,

$$R_0(B^+ \rightarrow K^{*0}\rho^+) = 0.50 \pm 0.19(\text{stat.})_{-0.07}^{+0.05}(\text{syst.}),$$

where the systematic error is associated with the fitting procedure determined by shifting each parameter by $\pm 1\sigma$, changing the PDF, and taking the quadratic sum of the resulting changes in R_0 as the systematic error.

We use the mass fit result and MC-determined efficiencies weighted by the measured polarization components to calculate the branching fraction for $B^+ \rightarrow K^{*0}\rho^+$; for the calculation of the upper limit of $B^0 \rightarrow K^{*0}\rho^0$, 100% longitudinal polarization is assumed.

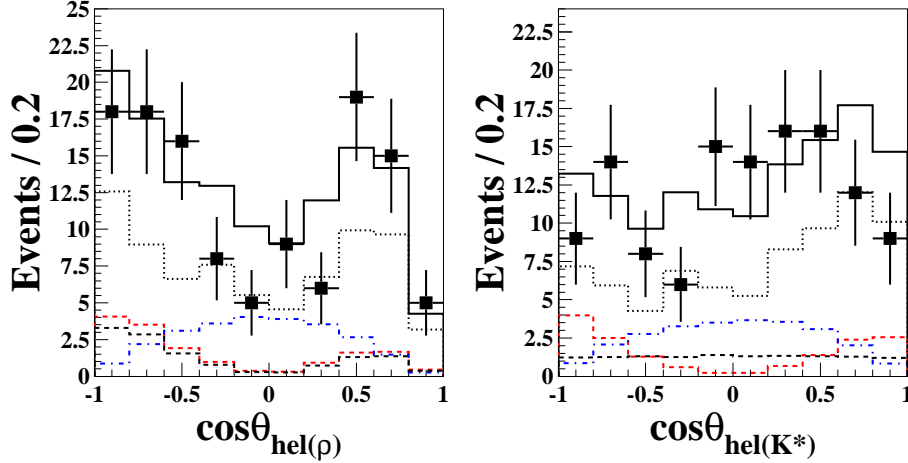


FIG. 4: Projections to $\cos \theta_{\text{hel}(\rho)}$ (left) and $\cos \theta_{\text{hel}(K^*)}$ (right). The solid histograms show the results of the two-dimensional fit. The red dashed (blue dot-dashed) histograms are the A_0 (A_{\pm}) component of the fit; The dotted histograms are backgrounds from continuum and $B\bar{B}$. The black dashed histograms are for non-resonant $\rho K \pi$. The low event yield near $\cos \theta_{\text{hel}(\rho)} = 1$ is due to the $p_{\pi^0} > 0.4 \text{ GeV}/c$ requirement.

We consider systematic errors in the branching fraction of the decay $B \rightarrow K^* \rho$ that are caused by uncertainties in the efficiencies of track finding, particle identification, π^0 reconstruction, continuum suppression and fitting. We assign a 1.1%/track error for the uncertainty in the tracking efficiency. This uncertainty is obtained from a study of partially reconstructed D^* decays. We also assign a 0.6%/track error for the particle identification efficiency that is based on a study of kinematically selected $D^{*+} \rightarrow D^0 \pi^+$, $D^0 \rightarrow K^- \pi^+$ decay. A 4.0% systematic error for the uncertainty in the π^0 detection efficiency is determined from data-MC comparisons of $\eta \rightarrow \pi^0 \pi^0 \pi^0$ with $\eta \rightarrow \pi^+ \pi^- \pi^0$ and $\eta \rightarrow \gamma \gamma$. A 3.4% ($K^{*0} \rho^0$)/3.8% ($K^{*0} \rho^+$) systematic error for continuum suppression is estimated from studying $B^+ \rightarrow D^- \pi^+$, $D^- \rightarrow K^- \pi^+ \pi^-$ and $B^+ \rightarrow \bar{D}^0 \pi^+$, $\bar{D}^0 \rightarrow K^+ \pi^- \pi^0$. A 3.8% systematic error associated with the $K^{*0} \rho^+$ fit is obtained by shifting the parameters by $\pm 1\sigma$ and changing the PDF. A fit systematic error of 16.1% for $K^{*0} \rho^0$ and 7.8% for $f_0(980) K^{*0}$ is found by varying the fit parameters by $\pm 1\sigma$. A 0.5% error for the uncertainty in the number of $B\bar{B}$ events in the data sample is also included. For $B^+ \rightarrow K^{*0} \rho^+$, we also include a 11.9% error due to the uncertainty in the fraction of longitudinal polarization. The quadratic sum of all of these errors is taken as the total systematic error. We obtain the branching fraction

$$\mathcal{B}(B^+ \rightarrow K^{*0} \rho^+) = (6.6 \pm 2.2(\text{stat.}) \pm 0.8(\text{syst.})) \times 10^{-6},$$

and set 90% confidence level (C.L.) upper limits on $B^0 \rightarrow K^{*0} \rho^0$,

$$\mathcal{B}(B^0 \rightarrow K^{*0} \rho^0) < 2.6 \times 10^{-6},$$

and $B^0 \rightarrow f_0(980) K^{*0}$,

$$\mathcal{B}(B^0 \rightarrow f_0(980) K^{*0}) < 5.2 \times 10^{-6}.$$

In summary, we measure the branching fraction for $B^+ \rightarrow K^{*0} \rho^+$, set a 90% CL. upper limit on $B^0 \rightarrow K^{*0} \rho^0$ and $B^0 \rightarrow f_0(980) K^{*0}$. A helicity analysis is performed for $B^+ \rightarrow$

$K^{*0}\rho^+$. We find a substantial transversely polarized fraction. The results are consistent with some recent calculations [3, 15]. All results reported here are preliminary.

We thank the KEKB group for the excellent operation of the accelerator, the KEK Cryogenics group for the efficient operation of the solenoid, and the KEK computer group and the National Institute of Informatics for valuable computing and Super-SINET network support. We acknowledge support from the Ministry of Education, Culture, Sports, Science, and Technology of Japan and the Japan Society for the Promotion of Science; the Australian Research Council and the Australian Department of Education, Science and Training; the National Science Foundation of China under contract No. 10175071; the Department of Science and Technology of India; the BK21 program of the Ministry of Education of Korea and the CHEP SRC program of the Korea Science and Engineering Foundation; the Polish State Committee for Scientific Research under contract No. 2P03B 01324; the Ministry of Science and Technology of the Russian Federation; the Ministry of Education, Science and Sport of the Republic of Slovenia; the National Science Council and the Ministry of Education of Taiwan; and the U.S. Department of Energy.

* on leave from Fermi National Accelerator Laboratory, Batavia, Illinois 60510

† on leave from Nova Gorica Polytechnic, Nova Gorica

- [1] A. Datta, D. London, hep-ph/0303159 (2003).
- [2] D. London, N. Sinha, R. Sinha, Phys. Rev. D **69**, 114013 (2004); A. Datta, hep-ph/0406192 (2004).
- [3] A. L. Kagan, hep-ph/0407076 (2004); A. L. Kagan, hep-ph/0405134 (2004).
- [4] Y. Grossman, Int. J. Mod. Phys. A **19**, 907 (2004).
- [5] J. Zhang *et al.* (Belle Collaboration), Phys. Rev. Lett. **91**, 221801 (2003).
- [6] B. Aubert *et al.* (BaBar Collaboration), Phys. Rev. Lett. **91**, 171802 (2003).
- [7] K. F. Chen *et al.* (Belle Collaboration), Phys. Rev. Lett. **91**, 201801 (2003).
- [8] S. Kurokawa and E. Kikutani, Nucl. Instr. Meth. A **499**, 1 (2003).
- [9] A. Abashian *et al.* (Belle Collaboration), Nucl. Instr. and Meth. A **479**, 117 (2002).
- [10] G.C. Fox, S. Wolfram, Phys. Lett. B **41**, 1581 (1978); K. Abe *et al.* (Belle Collaboration), Phys. Rev. Lett. **87**, 101801 (2001).
- [11] K. Abe *et al.* (Belle Collaboration), Phys. Rev. Lett. **87**, 091802 (2001);
- [12] J.E. Gaiser *et al.* (Crystal Ball Collaboration), Phys. Rev. D **34**, 711 (1986).
- [13] H. Albrecht *et al.* (ARGUS Collaboration), Phys. Lett. B **241**, 278 (1990).
- [14] K. Hagiwara *et al.*, Phys. Rev. D **66**, 010001 (2002).
- [15] C. W. Bauer, D. Pirjol, I. Z. Rothstein, I. W. Stewart, hep-ph/0401188 (2004).